Spin Hamiltonian characterization and refinement for Pr^{3+}:$YAlO_3$ and Pr^{3+}:Y_2SiO_5

Marko Lovrić,* Philipp Glasenapp, and Dieter Suter†
Technische Universität Dortmund, Fachbereich Physik, DE-44221 Dortmund, Germany
(Received 31 October 2011; revised manuscript received 20 December 2011; published 24 January 2012)

Rare-earth ions in dielectric crystals play an important role in high-resolution laser spectroscopy and are interesting candidates for storing quantum states of photons. We characterize the praseodymium hyperfine interaction of the ground-state ($^3H_4$) and one excited-state ($^1D_2$) for two important compounds: praseodymium doped in yttrium aluminum perovskite and praseodymium doped in yttrium orthosilicate. The spin Hamiltonian parameters are determined by numerical analysis of Raman-heterodyne spectra, which were collected for a range of static external magnetic field strengths and orientations. For Pr^{3+}:$YAlO_3$, we present a full analysis without restrictions for the Zeeman and quadrupole tensors, and our new characterization for Pr^{3+}:Y_2SiO_5 resolves a controversy in the literature.

DOI: 10.1103/PhysRevB.85.014429 PACS number(s): 76.30.Kg, 42.50.Md, 76.70.Hb, 76.60.−k

I. INTRODUCTION

Rare-earth ion-doped crystals (REIC) were shown to be interesting candidates for optical storage applications.[1] More recently, several studies also demonstrated their potential for physical implementations of quantum information and communication devices using photonic states. Achieved milestones include controlled phase gates[2] and single qubit arbitrary rotations.[3] A number of proposed schemes for efficient quantum memories[4–8] were demonstrated in prototype systems.[9–13] To achieve storage times beyond the optical dephasing time these schemes include a transfer of the input photon's quantum information into the longer lived hyperfine levels of the electronic ground-state.

The longest coherence lifetimes of solid-state rare-earth ions so far were observed in Pr^{3+}:Y_2SiO_5.[14] Using a combination of RF (radio frequency) decoupling pulses[15] and the so-called zero-first-order Zeeman (ZEFOZ) technique,[16] Fraval *et al.*[14] could increase the natural coherence lifetime of 500 μs to more than 30 s. The same techniques also allowed for a demonstration of stopped light based on electromagnetically induced transparency,[17–19] with storage times of more than one second.[20] In both cases, to reach this impressive timescales, the ZEFOZ technique was a crucial prerequisite. Its decoupling effect is based on a magnetic field that is chosen such that one Pr^{3+} ground-state transition frequency is independent of the Zeeman shift to first-order in the field. This effectively removes the dephasing effect of magnetic moment fluctuations, e.g., due to spins of the crystal host.[16]

Besides long coherence times, the implementations of quantum memories require precise optical control operations. In REIC, the relative optical transition strengths are determined by the specific tensor orientations of the ground- and excited-state spin Hamiltonian.[22] Investigating pure optical spectral tailoring techniques in Pr^{3+}:Y_2SiO_5, Nilsson *et al.*[23] found relative optical transition strengths that did not agree with those of Longdell *et al.*.[21] To solve this important controversy, we decided to perform an independent characterization of Pr^{3+}:Y_2SiO_5 and extract improved parameters of the spin Hamiltonian.

Apart from specific applications, the special properties REIC contributed to the basic understanding of optical spectra from solids[24] and later, especially with the invention of the laser, to the development of various high-resolution spectroscopic techniques.[22,25] In this context, Pr^{3+}:$YAlO_3$ was often chosen as testbed system due to its relatively narrow optical linewidth and strong optical transitions.[26]

In these low-symmetry REICs, the hyperfine interaction is quenched, but contributes to the nuclear spin Hamiltonian in second-order perturbation theory. Since the operator form of these effective Hamiltonians includes terms that are linear and quadratic in the nuclear spin operators, they cannot be distinguished from the normal Zeeman and quadrupole Hamiltonians. Accordingly, they are usually included in an enhanced nuclear Zeeman and an effective quadrupole operators.[27,28] In crystals with orthorhombic or higher crystal field symmetry at the praseodymium site, the orientation of the tensors is determined by the symmetry operations of the site and therefore it is identical for the Zeeman and quadrupole tensors. If the symmetry is lower, the principal axis systems (PAS) are not determined by symmetry and therefore, in general, it is different for the two tensors. The tensor orientation must be known, however, to calculate the relative optical transition strengths and the Zeeman shifts.

Although the site symmetry in $YAlO_3$ is lower (C_{1h}), previous studies of Pr^{3+}:$YAlO_3$ assumed that the effective quadrupole and Zeeman tensors have the same PAS. The latter approximation was based on the good agreement of the PAS's of the quadrupole and Zeeman tensors in the ground-state of Pr^{3+}:$YAlO_3$.[29] However, this approximation was known to be poor for the excited-state.[22,29] Here, we do not make this assumption. Our characterization therefore provides an independent measurement of the two tensor orientations. This results in much better fits between theoretically predicted line positions and transition amplitudes with experimental data.

II. SYSTEM AND HAMILTONIAN

The Hamiltonian for many rare-earth-doped compounds is well approximated by[22]

$$\mathcal{H}_0 = (\mathcal{H}_{FI} + \mathcal{H}_{CF}) + (\mathcal{H}_{HF} + \mathcal{H}_Q + \mathcal{H}_Z + \mathcal{H}_z). \quad (1)$$

The first two terms, the free ion (including spin-orbit coupling) and the crystal field Hamiltonians determine the energies of the electronic degrees of freedom. The lowest electronic

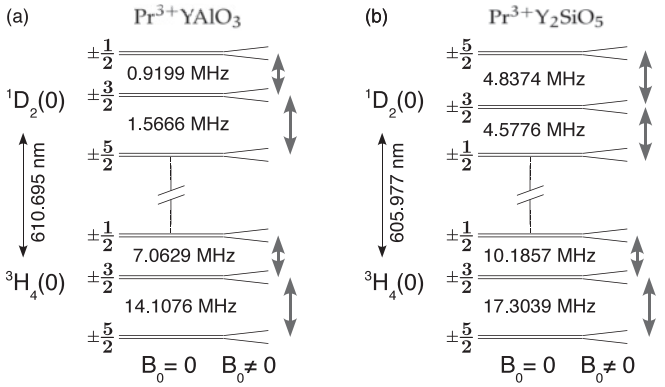

FIG. 1. Level structure for the lowest (0) $^3H_4$ and $^1D_2$ crystal field manifolds of (a) Pr^{3+}:$YAlO_3$ and (b) Pr^{3+}:Y_2SiO_5, including their hyperfine structure. The order of the energy levels follows from Refs. 30 and 31 and, respectively, Refs. 23 and 32, whereas the hyperfine transition frequencies given above follow from the present work. The arrows on the right indicate the range of hyperfine transitions excited by RF in the separate experiments. In (b), all excited-state transitions are excited in a single experiment.

ground-state $^3H_4(0)$ and the lowest level of the excited-state $^1D_2$ are defined by this terms of the Hamiltonian and represent the optical transition in our experiments.

The terms in the second bracket, describing the hyperfine coupling, the nuclear quadrupole coupling, the electronic and the nuclear Zeeman Hamiltonian, represent the spin Hamiltonian, whose characterization is the matter of this paper. The spin Hamiltonian lifts the degeneracy with respect to the nuclear spin and splits it up into $2I+1$ states in the presence of a magnetic field. Figure 1 shows the resulting level structures for the two compounds investigated, both doped with ^{141}Pr ($I=\frac{5}{2}$), which is the active rare-earth ion in our study.

A. The $YAlO_3$ system

Pr^{3+}:$YAlO_3$ forms an orthorhombic crystal of space group $P_{nma}(D_{2h}^{16})$.[33,34] The Pr ions substitute for the Y at four positions in each unit cell, which have C_{1h} point symmetry. The four positions are pairwise equivalent and the two pairs are related by a C_2 rotation around the crystal's b axis.[35] Taking this into account results in simplifying restrictions for the tensor orientations, as will be discussed later.

B. The Y_2SiO_5 system

The crystal structure of Pr^{3+}:Y_2SiO_5 is monoclinic with space group C_2/c (C_{2h}^6). Again, the Pr substitutes for the eight Y sites. In this case, four of the sites have different electronic energies; in the literature, they are referred to as the crystallographic "site 1" and "site 2."[36] In the context of this work, we consider only the crystallographic "site 1," whose optical transition is at $\lambda = 605.977$ nm.[36] Within this crystallographic "site 1," the site symmetry is only C_1 (see Ref. 36). The Pr are again pairwise equivalent and the pairs are related by a C_2 rotation around the crystal b axis.[21] In analogy to the Pr^{3+}:$YAlO_3$ system and in agreement with common terminology in the literature, we will refer to subsite 1 of the crystallographic "site 1" simply as site 1.

C. Spin Hamiltonian

In second-order perturbation theory, the nuclear spin part of $\mathcal{H}_0$ for our systems can be described by the following Hamiltonian:[22,27]

$$\mathcal{H}_1 = \vec{B}\cdot\mathbf{M}_1\cdot\vec{I} + \vec{I}\cdot\mathbf{Q}_1\cdot\vec{I}. \tag{2}$$

Here, the index 1 indicates that we refer to site 1. $\vec{I}$ denotes the vector of nuclear spin operators and $\vec{B}$ is the magnetic field vector. $\mathbf{M}$ describes an effective Zeeman tensor and $\mathbf{Q}$ the effective quadrupole tensor.

To determine the different parameters of this Hamiltonian, we measure the transition frequencies between the nuclear spin eigenstates as a function of amplitude and orientation of the magnetic field. For the subsequent analysis, we have to choose a common coordinate system for all tensors and operators. For this purpose, we choose the laboratory system, defined by the axes (x,y,z) of the magnetic field coils. The transformation between the principal axis systems of the tensors and the laboratory system can be written in terms of rotation matrices defined by Euler angles[37,38] $R_i = R(\alpha_i,\beta_i,\gamma_i)$:

$$\mathbf{M}_1 = R_M\cdot\begin{bmatrix} g_x & 0 & 0\\ 0 & g_y & 0\\ 0 & 0 & g_z\end{bmatrix}\cdot R_M^T, \tag{3}$$

$$\mathbf{Q}_1 = R_Q\cdot\begin{bmatrix} E-\frac{1}{3}D & 0 & 0\\ 0 & -E-\frac{1}{3}D & 0\\ 0 & 0 & \frac{2}{3}D\end{bmatrix}\cdot R_Q^T. \tag{4}$$

We now relate the Hamiltonian for site 2 with the help of the C_2 symmetry to $\mathcal{H}_1$ (2):

$$\mathcal{H}_2 = \vec{B}\cdot\left(R_{C_2}\mathbf{M}_1R_{C_2}^T\right)\cdot\vec{I} + \vec{I}\cdot\left(R_{C_2}\mathbf{Q}_1R_{C_2}^T\right)\cdot\vec{I}. \tag{5}$$

Here, R_{C_2} is the π rotation around the C_2 axis, whose orientation is defined by the angles α_{C_2} and β_{C_2} (see Ref. 39):

$$R_{C_2} = R_C^T\cdot R_\pi\cdot R_C,$$
$$R_C = R\left(\alpha_{C_2},\beta_{C_2},0\right),\quad R_\pi = R\left(180^\circ,0,0\right).$$

The tensor orientations and principal values depend on the local crystal field. Since the crystal field depends also on the electronic state, the eigenvalues and eigenstates are different for the electronic ground-state $^3H_4$ and the excited-state $^1D_2$ in both systems. Therefore the complete nuclear spin Hamiltonians of the two sites in a given electronic state depend on 13 parameters: $D,E,\alpha_Q,\beta_Q,\gamma_Q,g_x,g_y,g_z,\alpha_M,\beta_M,\gamma_M,\alpha_{C_2}$, and β_{C_2}.

III. EXPERIMENTAL SETUP AND MEASUREMENT PROCEDURE

The dopant level of Pr^{3+} was 0.1% at. for Pr^{3+}:$YAlO_3$ and 0.05% at. for the Pr^{3+}:Y_2SiO_5 crystal. Both samples were of high optical quality and had dimensions of $5\times5\times1$ mm. We mounted the crystals in an optical cold-finger cryostat operated at liquid helium temperatures. The laser beam direction, which is aligned with the z axis, was oriented perpendicular to the 5×5 mm surface by back reflection. For Pr^{3+}:$YAlO_3$, the crystal axes are perpendicular to the polished crystal surfaces, and we aligned the crystal such that they were parallel to the laboratory axes: $x\parallel b$, $y\parallel a$, and $z\parallel c$. Since Pr^{3+}:Y_2SiO_5 is monoclinic, we aligned its optical axes as reference with

the laboratory reference axes: $x \parallel D2$, $y \parallel D1$, and $z \parallel b$ (we note that in Ref. 21, the crystal b axis was aligned along the laboratory y axis). As we will give all results in laboratory coordinates, mounting precision translates into the angles α_{C_2} and β_{C_2} deviating slightly from the theoretical values, but does not increase the errors of the other Hamiltonian parameters.

To collect experimental data of both, the electronic ground-state and the electronically excited-state, we used hyperfine spectra obtained by the Raman-heterodyne scattering (RHS) technique.[40,41] Figure 1 shows the relevant states for the two samples. The frequencies in the figure refer to the zero-field splitting. In the magnetic field, the relevant transitions are spread over a range of ≈1 to 10 MHz around these values.

For all experiments, we first create initial population differences between the hyperfine states by irradiating them with a resonant laser. For both samples,[36,42] the optical homogenous linewidth is much smaller than inhomogeneous broadening of the $^3H_4 \leftrightarrow {}^1D_2$ transition. Therefore the laser preparation causes hole-burning effects and partial polarization of groups of Pr^{3+} ions of the same transition frequency and all hyperfine transitions are visible in a single RHS spectrum. A resonant RF field, applied along the z axis, then created coherences between the hyperfine levels. We used pulsed RF fields for the excited-state and chirped CW (continuous wave) RF for the ground-state experiments. The spectra were centered around the zero-field hyperfine frequency indicated in Fig. 1. To detect the hyperfine coherence, a weak resonant laser transfers them into the optical transitions. At the same time, the weak laser serves as the local oscillator for a heterodyne detection of the Raman field, which is emitted into the same optical mode. Our laser source was a Coherent 899-21 dye laser, further stabilized by homebuilt electronics to a linewidth ≲20 kHz on timescales shorter than 10 ms.

To determine the tensor orientations, spectra were collected for different applied magnetic fields. To generate the fields, we used three orthogonal pairs of coils in Helmholtz configuration. We controlled the field by calibrated Hall probes and a computer-based feedback-loop, compensating for drifts and nonlinearities. The resulting absolute error of the field components was less than 0.06 mT and the relative linear error less than 0.3%. To obtain a uniform sampling of the orientational dependence of the RHS spectra, we varied the magnetic field along a spiral on the surface of an ellipsoid:[21,39]

$$\vec{B}(t) = \begin{pmatrix} B_x\sqrt{1-t^2}\cos(6\pi t) \\ B_y\sqrt{1-t^2}\sin(6\pi t) \\ B_z t \end{pmatrix}, \qquad (6)$$

with

$$t = -1 + (N-1)\frac{2}{N_{\rm tot}-1}, \quad N = 1,2,\ldots,N_{\rm tot}.$$

For the ground-state of Pr^{3+}:$YAlO_3$, we measured $N_{\rm tot} = 151$ orientations, with magnetic field magnitudes of $[B_x, B_y, B_z] = [9.5, 11, 10.5]$ mT and for the excited-state, we used $N_{\rm tot} = 101$ and $B_x = B_y = B_z = 6.5$ mT. In the case of Pr^{3+}:Y_2SiO_5, we used $N_{\rm tot} = 250$ orientations and magnetic field amplitudes $[B_x, B_y, B_z] = [9.5, 11, 10.5]$ mT for both states. More details on the experimental setup can be found in our recently published study investigating the compound $Pr^{3+}La_2(WO_4)_3$.[39]

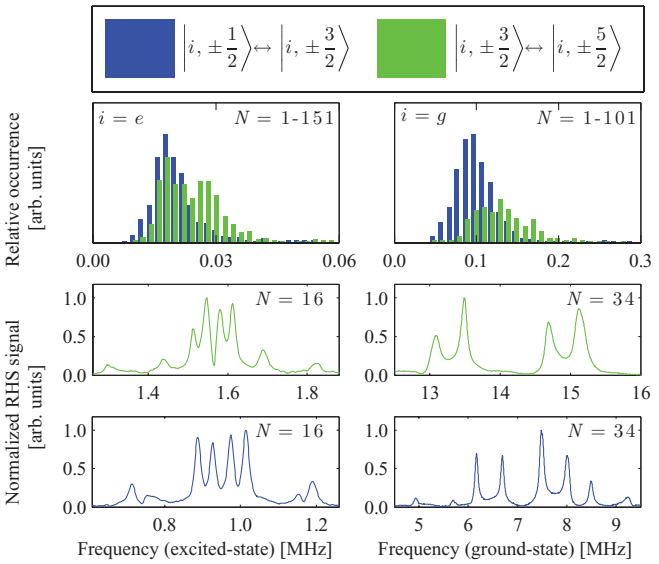

FIG. 2. (Color online) Linewidth histograms and representative RHS spectra of the ground- and exited-state of Pr^{3+}:$YAlO_3$. The histograms on the top show the distributions of fitted full width at half maximum (FWHM) RHS linewidths for all recorded data, plotted separately for the two hyperfine transitions. We recorded both spectra from the ground-state at $N = 16$, corresponding to $\vec{B} = (-3.35, 8.25, -5.88)$ mT. For the excited-state spectra we used $\vec{B} = (3.76, -2.73, -4.55)$ mT. The vertical scale of each spectrum is normalized to the largest line.

IV. SPECTRA AND DATA ANALYSIS

Figures 2 and 3 show some typical experimental RHS spectra for the ground- and excited-state of both compounds. For the applied magnetic fields, the transition frequencies of the hyperfine manifolds $|i, \pm\frac{1}{2}\rangle \leftrightarrow |i, \pm\frac{3}{2}\rangle$ and $|i, \pm\frac{3}{2}\rangle \leftrightarrow |i, \pm\frac{5}{2}\rangle$ ($i = g$ or e) do not overlap for both electronic state of Pr^{3+}:$YAlO_3$ and for the Pr^{3+}:Y_2SiO_5 ground-state spectra. We therefore plot these manifold spectra separately. They contain $4 + 4$ lines from the two Pr sites, except when overlap occurs. In some cases, the transition strengths are so small that they become unobservable. To avoid an influence of RF phase distortions, we use absolute value spectra in general. We fitted Gaussians to the RHS lines to extract their frequency, amplitude and inhomogeneous widths. The distribution of the linewidths for all recorded spectra and field orientations is plotted in histograms above the corresponding spectra.

A. Pr^{3+}:$YAlO_3$ spectra

The mean linewidths of the Pr^{3+}:$YAlO_3$ ground-state spectra are $|g, \pm\frac{1}{2}\rangle \leftrightarrow |g, \pm\frac{3}{2}\rangle \approx 104$ kHz, $|g, \pm\frac{3}{2}\rangle \leftrightarrow |g, \pm\frac{5}{2}\rangle \approx 134$ kHz. The corresponding values for the excited-state are, in the same sequence, ≈21.1 and 24.7 kHz. As can also be seen in the single histograms of Fig. 2, the linewidths of the $|i, \pm\frac{3}{2}\rangle \leftrightarrow |i, \pm\frac{5}{2}\rangle$ are larger than those of the $|i, \pm\frac{1}{2}\rangle \leftrightarrow |i, \pm\frac{3}{2}\rangle$ manifolds. We have observed the same

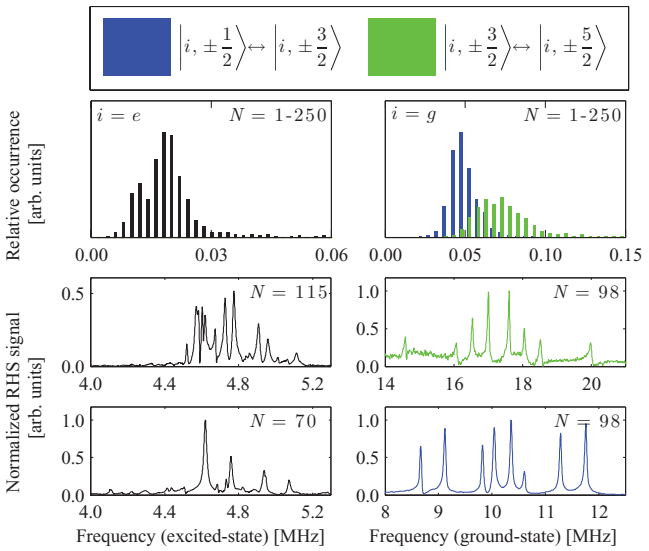

FIG. 3. (Color online) Linewidth histograms and representative RHS spectra for Pr^{3+}:Y_2SiO_5. The ground-state spectra correspond to $\vec{B} = (-4.83, 9.15, -2.32)$ mT and for the excited-state we plot two spectra for different fields, with $\vec{B} = (-4.44, -8.40, -4.68)$ mT for $N = 70$ and $\vec{B} = (-0.18, -10.96, -0.89)$ mT for $N = 115$, respectively. The vertical scale of each ground-state spectrum is normalized to one, those of the excited-state to the largest line of the full data set.

effect in $Pr^{3+}La_2(WO_4)_3$ previously and attribute it mainly to the approximately two times higher impact of the quadrupole constant D in the $|g, \pm\frac{3}{2}\rangle \leftrightarrow |g, \pm\frac{5}{2}\rangle$-Hamiltonian matrix elements.[39] The lower separation of the bimodal shape for the linewidth distribution observed in Pr^{3+}:$YAlO_3$ is compatible with the assumption that the widths also scale with the magnitude of quadrupole coupling.[39] As an example, the ratio of the quadrupole coupling constants in the electronic ground-states is $D(Pr^{3+}La_2(WO_4)_3) \approx 1.8D(Pr^{3+} : YAlO_3)$ (see Table I).

B. Pr^{3+}:Y_2SiO_5 spectra

In Pr^{3+}:Y_2SiO_5, the excited-state hyperfine manifolds are only separated by about 260 kHz in zero field. Static magnetic fields of approximately 10 mT therefore generate almost complete overlap of their RHS spectra. For the statistical analysis, we did not separate them and the histogram shows both excited-state hyperfine manifolds binned together (black) in Fig. 3. The excited-state spectra thus contain at most 16 lines. To reduce the impact of small amplitudes, line distortion and overlap (compare, e.g., $N = 70$ and 115 spectra), we did not include lines with amplitudes less than 0.15 or widths greater than 67 kHz in the fitting procedure. The histogram for the excited-state also excludes these lines.

The mean linewidth for the ground-state Pr^{3+}:Y_2SiO_5 RHS lines is approximately 50.5 kHz for the $|g, \pm\frac{1}{2}\rangle \leftrightarrow |g, \pm\frac{3}{2}\rangle$ transitions and approximately 75.4 kHz for the $|g, \pm\frac{3}{2}\rangle \leftrightarrow |g, \pm\frac{5}{2}\rangle$ transitions. For the excited-state, we found a mean of about 18.9 kHz, with the bimodal peaks at approximately 12 and 18 kHz. The bimodal structure was found in both electronic states, the separation being slightly higher than in the case of Pr^{3+}:$YAlO_3$.

TABLE I. Pr^{3+}:$YAlO_3$ best fit parameters and fit errors. D and E are given in MHz, the $g_{\alpha'}$ values in MHz/T, all angles in degrees and the resulting RMS deviation $f_{\text{best}}^{\text{RMS}}$ is given in kHz. For D, E, and the $g_{\alpha'}$ the errors are given in relative units. For the ground-state spectra, we used the value of $\nu_\sigma^{\text{SNR}} = 545$ kHz [see Eq. (7)], which yielded $\nu_\sigma^{\text{STD}} = 13$ Hz, and for the excited-state, $\nu_\sigma^{\text{SNR}} = 248$ Hz and $\nu_\sigma^{\text{STD}} = 8$ Hz.

	ground-state			excited-state		
	value	$\sigma_{\nu_\sigma^{\text{SNR}}}$	$\sigma_{\nu_\sigma^{\text{STD}}}$	value	$\sigma_{\nu_\sigma^{\text{SNR}}}$	$\sigma_{\nu_\sigma^{\text{STD}}}$
D	−3.5276	0.6%	0.1%	−0.40211	1.3%	0.2%
E	−0.037	54%	6%	−0.050463	11.2%	0.4%
α_Q	−88	17	3	1.6	1.0	0.2
β_Q	88.49	0.37	0.07	89.24	0.54	0.08
γ_Q	118.55	0.56	0.09	99.82	0.39	0.08
g_x	36.99	3.4%	0.5%	16.769	3.97%	0.04%
g_y	25.6	5.8%	0.9%	13.06	2.1%	0.4%
g_z	117.59	0.61%	0.10%	18.475	1.32%	0.04%
α_M	1.9	2.7	0.5	1.3238	2.5207	0.0003
β_M	88.33	0.25	0.04	86.58	5.34	0.01
γ_M	122.36	0.26	0.04	146.12	1.11	0.03
α_{C_2}	2.18	0.17	0.03	1.85	0.27	0.06
β_{C_2}	88.00	0.27	0.05	88.3	0.6	0.1
$f_{\text{best}}^{\text{RMS}}$	15.90	0.78	0.02	2.381	0.351	0.009

C. Data reduction

To prepare the data for the fitting procedure, we identified the center frequencies and widths of all usable spectral lines by fitting Gaussians to them. In spectra where many lines with different amplitudes overlap, we partially used the line maxima as reference for their centers. If the lines were strongly distorted, we did not include them in the data analysis.

By calculating the eigenvalues of the Hamiltonians (2) and (5) for a given set of trial parameters, we calculated theoretical frequencies for the RHS lines and used them for the fitting algorithm. Due to the large parameter space (13 in total for each state) and their complicated interdependence, gradient-based fitting algorithms are not efficient, as they tend to remain locked in local minima. As in the work of Longdell *et al.*,[21,43] we used simulated annealing[44] to minimize the RMS (root mean square) deviation between measured and theoretical frequencies. This resulted in a robust convergence to the global minimum. More specific details on the fitting procedure can be found in our recently published study investigating the compound $Pr^{3+}La_2(WO_4)_3$.[39]

When using RHS spectra to determine the hyperfine Hamiltonians, one has to take into account the symmetry operations that leave the spectra invariant. For example if the signs of D and E are inverted simultaneously, all spectra remain invariant. The same holds true for a simultaneous inversion of the signs of g_x, g_y, and g_z. Therefore we use the literature values for the signs of the tensor principal values.[23,30–32] Other intrinsic ambiguities, e.g., different sets of Euler angles giving the same tensor orientation, are a matter

of convention and do not influence the results presented in the next sections.

V. Pr^{3+}:$YAlO_3$ RESULTS AND DISCUSSION

A. Procedure and results

The RHS line identification resulted in 1607 lines for the ground-state data, of which 1599 were uniquely identified with theoretically predicted transition frequencies. For the excited-state 1153 of 1168 lines were identified in the same way. Table I and Fig. 4 show the fit results and the measured RHS spectra.

The remaining deviation between experimental data and fitted resonance positions was 15.9 kHz for the ground-state. This represents a very high model accuracy, since the average linewidth (see Fig. 3) of the underlying RHS lines is about seven times higher. The excited-state results are of even better quality, since the mean deviation of 2.38 kHz is 10 times smaller than the mean linewidth.

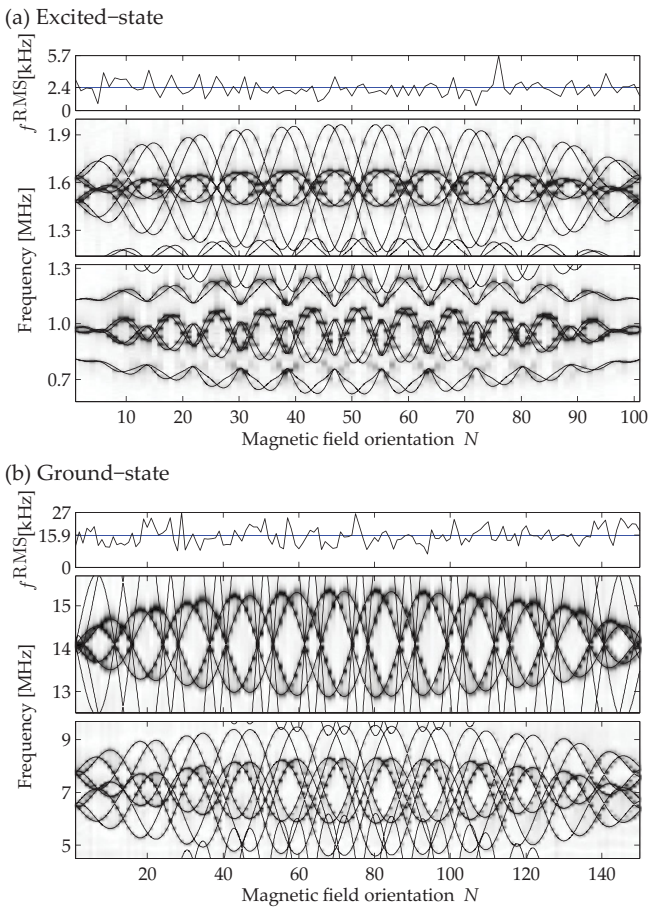

FIG. 4. (Color online) Pr^{3+}:$YAlO_3$ RHS data and overlaid fit. The RHS data are shown as a grayscale coded intensity plot. The maximum amplitude for each individual spectrum (indexed by N) was normalized to one, in order to obtain a uniform contrast over all orientations. The calculated line positions [using Table I and Eqs. (2) and (5)] are given by the overlaid black lines. Additionally, the RMS deviations f^{RMS} for the N individual orientations are plotted [black line in (a) and (b) top row plots]. The blue horizontal line indicates the mean value (see Table I) of the deviations.

This and the lack of systematic deviations for the individual spectra (see Fig. 4) over the whole range of magnetic fields, indicates that the residual deviation is of statistical origin. Table I lists the resulting spin Hamiltonian parameters for Pr^{3+}:$YAlO_3$.

To estimate the uncertainty of the fitted parameters, we let the simulated annealing run at two different, low temperatures. Such a procedure samples the sensitivity of fitted parameters in the vicinity of the found global minimum and allows to estimate their error.[39] For a temperature that results in the $\sigma_{\nu_\sigma}^{SNR}$ error, we chose a level of uncertainty for the line positions that corresponds to the mean ratio of fitted linewidths σ_i to the individual signal-to-noise ratio (SNR_i) for all contributing RHS lines:[39]

$$\nu_\sigma^{SNR} = \frac{1}{L}\sum_{i=1}^{L}\frac{\sigma_i}{SNR_i}. \tag{7}$$

The resulting errors, which are listed in Table I, tend to be too large, since the chosen temperature corresponds to the worst case, when all lines are globally shifted in the same way. The second error, $\sigma_{\nu_\sigma}^{STD}$, uses a temperature that follows from random shifts by $\pm\nu_\sigma^{SNR}$ on all individual lines. It thus resembles the statistical error of the fit, assuming only random noise in the line positions.

Apart from the fitting error, we also have to consider systematic errors. We estimate a calibration error of the magnetic field of approximately 0.65%, which translates to the same fractional uncertainty of the gyromagnetic ratios g_x, g_y, and g_z. As the parameters are given in the laboratory-fixed reference frame (x,y,z) a misalignment of the crystal does not contribute to the error but is expressed by the α_{C_2} and β_{C_2} values not being exactly 0 or 90°. A systematic contribution in the angles arises from a possible nonorthogonality of the coils, which we estimate to be less than 1°. For the error of the angles seen relative to the crystal axis system, we estimate to be about 5° based on the typical precision for the x-ray characterization, cutting and polishing procedure for the the crystal surfaces.

B. Disscussion

Due to the C_{1h} site symmetry in Pr^{3+}:$YAlO_3$, the tensors of the ground- and excited-state share a common quantization axis,[29] which is the crystal c axis. This implies that the tensors' principal z axes lie in the crystal a-b plane. In this case, the relative angle between the **Q**-PAS z axes of the ground- and excited-states is sufficient to determine the overlap integrals of the nuclear spin states in zero field.[22,45,46] Figure 5 shows the orientation of the principal z axes for the **Q** and **M** tensors following from Table I. As mentioned before, the RHS signal is insensitive to inversion of the signs of the quadrupole coupling constants or of the gyromagnetic ratios. Therefore in the figure, we only draw the orientation of the axes and quote the smallest angles connecting them. Further, we draw the axes for the situation where the site 1 of the ground-state is correlated with the site 2 results of the excited-state. The RHS scheme does not correlate a given Pr^{3+} site from the ground-state with a specific site of the excited-state.[30] Out of the two possible assignments, we draw the situation where the quadrupole z axis

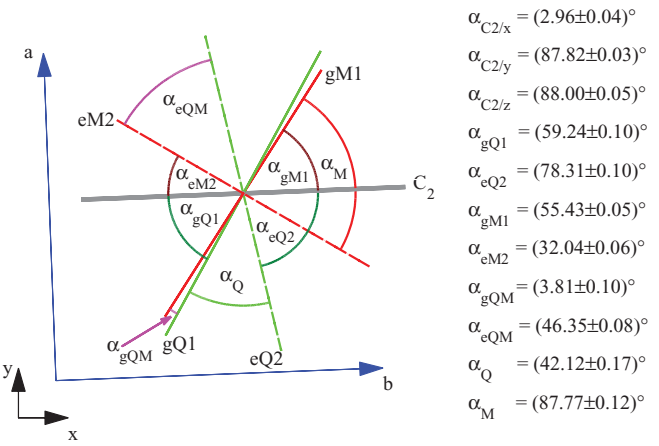

FIG. 5. (Color online) Orientation of the Pr^{3+}:$YAlO_3$ quadrupole and Zeeman principal axes. The LAS *x*-*y* plane is given by the black and the crystal *a*-*b* plane by the blue arrows ($C_2 \parallel b$). The green lines show the *z* axis of quadrupole tensors (gQ1, eQ2) and the red lines show the *z* axes of the corresponding Zeeman tensors (gM1, eM2). The angles between the C_2 and the LAS ($\alpha_{C2/x,y,z}$) axes are only given in the figure legend, the other relevant angles are drawn in the figure: the angles between the drawn axes and the C_2 axis (α_{gQ1}, α_{eQ2}, α_{gM1}, α_{eM2}), relative angles between the $\hat{Q}$ and $\hat{M}$ *z* axes within one state (α_{gQM} and α_{eQM}) and the mixing angles between the ground and excited $\hat{Q}$ and $\hat{M}$ tensor *z* axes (α_Q and α_M). The angles for site 1 follow from Table I and Eqs. (3)–(4) and site 2 additionally incorporates the C_2 transformation [see Eq. (5)]. Errors follow from propagation of the $\sigma^{\mathrm{STD}}_{\nu_\sigma}$ errors.

of the ground-state is rotated by an angle $\alpha_Q(gQ1/eQ2) = (42.1 \pm 0.2)^\circ$ with respect to the excited-state. This is in perfect agreement with studies that are sensitive to this angle: Ref. 47 giving $\alpha_Q = (47 \pm 5)^\circ$ and Ref. 46 yielding $\alpha_Q = (42 \pm 1)^\circ$.

Compared to the previous studies[26,29–31,35,45,48] of this compound, we use a more general spin Hamiltonian model, with independent PAS systems for the **Q** and **M** tensors. The result of our analysis yields an angle of $\alpha_{gQM} = (3.8 \pm 0.1)^\circ$ between the *z* axes of the **Q** and **M** tensors of the $^3H_4$ electronic ground-state—relatively close to zero used in the simpler earlier models.[26,29,35] In the $^1D_2$ excited-state, however, the corresponding angle is $\alpha_{eQM} = (46.4 \pm 0.1)^\circ$, clearly incompatible with the simple models used before.

We also compared the two models by performing an independent fit with the simple model (10 parameters) and calculated the RMS deviations f^{RMS} for the collected RHS spectra. For the ground-state, the best fit yielded a deviation of 23.2 kHz and for the excited-state, 12.6 kHz. Thus the more general model of the Pr^{3+}:$YAlO_3$ system reduces the error by a factor of more than five compared to the simple model used before. This result is of particular importance for experiments that require very precise prediction of the hyperfine levels for a given magnetic field (e.g., Refs. 14, 16, and 20) or need precise knowledge of relative transition strengths,[49] which depend on the relative orientation of the tensors in the ground- and excited-state.[22] Table II lists the relative oscillator strengths derived from the parameters in Table I at zero magnetic field.

The different orientations of the **Q** PAS (x',y',z') for the ground- and excited-states can be traced to the fact that the hyperfine interaction dominates the ground-state tensor, while it is much smaller in the excited-state.[29] Thus the nuclear quadrupole interaction becomes more important in the excited-state and determines the properties of the **Q** tensor.

We note that the Zeeman tensors **M** of the ground- and excited-states have almost identical orientation: the angles between the **M** tensor axes $\alpha(gM_{x''}/eM_{x''}) = (2.8 \pm 0.5)^\circ$,$\alpha(gM_{y''}/eM_{z''}) = (3.4 \pm 0.4)^\circ$, and $\alpha(gM_{z''}/eM_{y''}) = (2.6 \pm 0.1)^\circ$. The implicit exchange of the $y'' \leftrightarrow z''$ axes between ground- and excited-state is only a matter of convention.

VI. Pr^{3+}:Y_2SiO_5 RESULTS AND DISCUSSION

A. Procedure and results

For the ground-state of Pr^{3+}:Y_2SiO_5, 3209 of the 3212 identified RHS lines could be uniquely mapped to the theoretically predicted transitions. The residual deviation between the data and the fitted model is 7.48 kHz, which is about eight times smaller than the RHS inhomogenous linewidth, indicating an excellent fit between theoretical model and experimental data. The residual deviation is approximately three times lower than in an earlier characterization of Pr^{3+}:Y_2SiO_5 by Longdell *et al.*[21]

Due to the restriction to RHS lines with relative amplitudes greater than 0.15 and widths smaller than 67 kHz in the excited-state, the number of RHS lines left for the fitting was 1330. With the fitted model, 1297 of these could be uniquely identified with theoretical transitions, yielding a residual RMS deviation of 9.93 kHz. This is slightly worse than the 7 kHz

TABLE II. Relative oscillator strengths for Pr^{3+}:$YAlO_3$. The calculated values are derived from Table I (calc., site 1 values for the ground-state and site 2 values for the excited-state) are compared to the latest published values (lit.).[46] Rows correspond to transitions starting from the ground-state hyperfine levels and columns correspond to transitions to different excited-state hyperfine levels.

		$\lvert e, \pm\frac{1}{2}\rangle$	$\lvert e, \pm\frac{3}{2}\rangle$	$\lvert e, \pm\frac{5}{2}\rangle$
	calc.	0.244 ± 0.014	0.648 ± 0.005	0.109 ± 0.009
$\langle g, \pm\frac{1}{2}\rvert$	lit.	0.239	0.647	0.114
	calc.	0.541 ± 0.003	0.038 ± 0.009	0.421 ± 0.006
$\langle g, \pm\frac{3}{2}\rvert$	lit.	0.549	0.003	0.417
	calc.	0.215 ± 0.012	0.314 ± 0.004	0.471 ± 0.015
$\langle g, \pm\frac{5}{2}\rvert$	lit.	0.212	0.319	0.469

TABLE III. Pr^{3+}:Y_2SiO_5 best fit parameters and fit errors. D and E are given in MHz, the $g_{\alpha'}$ values in MHz/T, all angles in degrees and the resulting RMS deviation $f_{\text{best}}^{\text{RMS}}$ is given in kHz. For D, E, and the $g_{\alpha'}$ the errors are given in relative units. For the ground-state spectra, we found $\nu_\sigma^{\text{SNR}} = 535$ Hz, which yielded $\nu_\sigma^{\text{STD}} = 9.4$ Hz and for the excited-state, $\nu_\sigma^{\text{SNR}} = 101$ Hz and $\nu_\sigma^{\text{STD}} = 2.9$ Hz.

	ground-state			excited-state		
	value	$\sigma_{\nu_\sigma^{\text{SNR}}}$	$\sigma_{\nu_\sigma^{\text{STD}}}$	value	$\sigma_{\nu_\sigma^{\text{SNR}}}$	$\sigma_{\nu_\sigma^{\text{STD}}}$
D	−4.4435	0.35%	0.05%	1.35679	0.46%	0.08%
E	−0.56253	2.0%	0.20%	0.42192	1.3%	0.2%
α_Q	62.1	1.0	0.1	123.51	0.60	0.09
β_Q	31.81	0.23	0.03	94.69	0.33	0.06
γ_Q	93.94	0.61	0.07	170.56	0.39	0.7
g_x	26.57	3.3%	0.3%	14.54	3.3%	0.6%
g_y	31.01	3.4%	0.4%	14.30	2.1%	0.3%
g_z	113.08	0.32%	0.05%	33.76	1.2%	0.2%
α_M	112.0	4.7	0.6	44	26	6
β_M	35.68	0.14	0.02	63.91	0.38	0.07
γ_M	101.54	0.22	0.03	3.0	0.4	0.1
α_{C_2}	110.0	3.5	0.5	120	7	1
β_{C_2}	1.574	0.076	0.009	1.65	0.25	0.05
$f_{\text{best}}^{\text{RMS}}$	7.48	0.70	0.01	9.928	0.140	0.007

deviation reported in Ref. 21 but still represents a good fit, since the mean RHS inhomogenous linewidth is about twice this value. Table III and Fig. 6 show the fit results and the measured RHS spectra for both electronic states of Pr^{3+}:Y_2SiO_5.

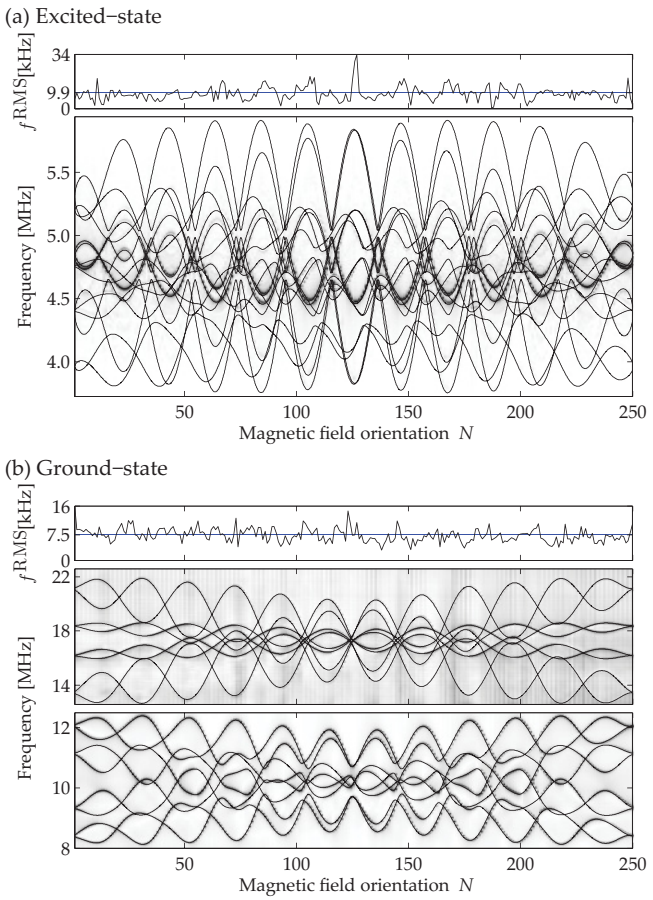

FIG. 6. (Color online) Pr^{3+}:Y_2SiO_5 RHS spectra as a function of magnetic field orientation as grayscale coded intensity plot and overlaid fit. For details of the presentation see the caption of Fig. 4.

B. Discussion

Since the Pr^{3+} site in Y_2SiO_5 has C_1 symmetry, the tensor axes are not restricted in this case; this is borne out by the experimental data. An analysis of the relative orientations is still useful, since they determine the overlap of the nuclear wave functions and therefore the relative optical oscillator strengths.[22] In Table IV, we give the relative oscillator strengths for all possible optical transitions for $B = 0$. The oscillator strengths of Pr^{3+}:Y_2SiO_5 were determined earlier by Nilsson *et al.*,[23] using pure optical spectral tailoring experiments. Their results did not agree with the relative oscillator strengths calculated from the nuclear overlaps of Longdell *et al.*.[21] It was assumed that an effect based on the Pr-Y hyperfine coupling is responsible for the controversy. Our characterization results yields relative oscillator strengths in perfect agreement with the relative optical oscillator strengths measured by Nilsson *et al.*.[23] We attribute the very good agreement primarily to a better fit of the excited-state tensor orientations, which may be connected to the more general set of magnetic field orientations we also used for the excited-state measurements [see Eq. (6)], in comparison to Ref. 21.

TABLE IV. Relative oscillator strengths for Pr^{3+}:Y_2SiO_5. The calculated values are derived from Table III (calc., site 1 for both states) are compared to values from spectral tailoring experiments (exp.).[23] Rows correspond to transitions starting from the ground-state hyperfine levels and columns correspond to transitions to different excited-state hyperfine levels.

		$\lvert e, \pm\frac{1}{2}\rangle$	$\lvert e, \pm\frac{3}{2}\rangle$	$\lvert e, \pm\frac{5}{2}\rangle$
	calc.	0.560 ± 0.004	0.373 ± 0.004	0.067 ± 0.001
$\langle g, \pm\frac{1}{2}\rvert$	exp.	0.55 ± 0.01	0.38 ± 0.01	0.07 ± 0.01
	calc.	0.399 ± 0.004	0.594 ± 0.004	0.007 ± 0.001
$\langle g, \pm\frac{3}{2}\rvert$	exp.	0.40 ± 0.01	0.60 ± 0.01	0.01 ± 0.01
	calc.	0.041 ± 0.001	0.033 ± 0.001	0.936 ± 0.002
$\langle g, \pm\frac{5}{2}\rvert$	exp.	0.05 ± 0.01	0.02 ± 0.01	0.93 ± 0.01

VII. CONCLUSION

In this study, we have characterized the spin Hamiltonians of two praseodymium-based compounds that have shown an interesting potential for photonic applications. We determined all relevant parameters of the nuclear spin Hamiltonians in the electronic ground-state as well as in one electronically excited-state. Not assuming that the principal axis systems of the Zeeman and the effective quadrupole tensors coincide, we obtained independent orientation parameters. In both compounds, our results allow calculations of transition frequencies and relative oscillator strengths for arbitrary magnetic field vectors with a precision exceeding the previous studies by far. Our characterization of Pr^{3+}:Y_2SiO_5 resolves a controversy from the literature: relative optical oscillator strengths that were obtained by pure optical techniques[23] were in conflict with results from a magnetic measurement,[21] but they are in perfect agreement with our results, which also used magnetic fields and nuclear spin transitions. Correct relative oscillator strengths are an important precondition for the implementation of quantum memories.

ACKNOWLEDGMENT

We thank Philippe Goldner for helpful discussions during the data analysis.

*marko.lovric@tu-dortmund.de
†dieter.suter@tu-dortmund.de

[1] T. W. Mossberg, Opt. Lett. **7**, 77 (1982).
[2] J. J. Longdell, M. J. Sellars, and N. B. Manson, Phys. Rev. Lett. **93**, 130503 (2004).
[3] L. Rippe, B. Julsgaard, A. Walther, Y. Ying, and S. Kröll, Phys. Rev. A **77**, 022307 (2008).
[4] M. Nilsson and S. Kröll, Opt. Commun. **247**, 393 (2005).
[5] M. Afzelius, C. Simon, H. deRiedmatten, and N. Gisin, Phys. Rev. A **79**, 052329 (2009).
[6] G. Hétet, J. J. Longdell, A. L. Alexander, P. K. Lam, and M. J. Sellars, Phys. Rev. Lett. **100**, 023601 (2008).
[7] R. Lauro, T. Chanelière, and J. L. LeGouët, Phys. Rev. A **79**, 053801 (2009).
[8] V. Damon, M. Bonarota, A. Louchet-Chauvet, T. Chanelière, and J.-L. L. Gouët, New J. Phys. **13**, 093031 (2011).
[9] M. Hedges, J. J. Longdell, Y. Li, and M. J. Sellars, Nature (London) **465**, 1052 (2010).
[10] I. Usmani, M. Afzelius, H. de Riedmatten, and N. Gisin, Nat. Commun. **1**, 1 (2010).
[11] M. Bonarota, J. L. Gouët, and T. Chanelière, New J. Phys. **13**, 013013 (2011).
[12] C. Clausen, I. Usmani, F. Bussières, N. Sangouard, M. Afzelius, H. D. Riedmatten, and N. Gisin, Nature (London) **469**, 508 (2011).
[13] E. Saglamyurek, N. Sinclair, J. Jin, J. A. Slater, D. Oblak, F. Bussières, M. George, R. Ricken, W. Sohler, and W. Tittel, Nature (London) **469**, 512 (2011).
[14] E. Fraval, M. J. Sellars, and J. J. Longdell, Phys. Rev. Lett. **95**, 030506 (2005).
[15] S. Meiboom and D. Gill, Rev. Sci. Instrum. **29**, 688 (1958).
[16] E. Fraval, M. J. Sellars, and J. J. Longdell, Phys. Rev. Lett. **92**, 077601 (2004).
[17] K.-J. Boller, A. Imamoglu, and S. E. Harris, Phys. Rev. Lett. **66**, 2593 (1991).
[18] S. Harris, Phys. Today **50**, 36 (1997).
[19] D. F. Phillips, A. Fleischhauer, A. Mair, R. L. Walsworth, and M. D. Lukin, Phys. Rev. Lett. **86**, 783 (2001).
[20] J. J. Longdell, E. Fraval, M. J. Sellars, and N. B. Manson, Phys. Rev. Lett. **95**, 063601 (2005).
[21] J. J. Longdell, M. J. Sellars, and N. B. Manson, Phys. Rev. B **66**, 035101 (2002).
[22] R. M. Macfarlane and R. M. Shelby, in *Spectroscopy of Solids Containing Rare Earth Ions*, Modern Problems in Condensed Matter Sciences Vol. 21, edited by A. A. Kaplyanskii and R. M. Macfarlane (North Holland, Amsterdam, 1987), pp. 51–184.
[23] M. Nilsson, L. Rippe, S. Kröll, R. Klieber, and D. Suter, Phys. Rev. B **70**, 214116 (2004).
[24] J. H. van Vleck, J. Phys. Chem. **41**, 67 (1937).
[25] R. Macfarlane, J. Lumin. **100**, 1 (2002).
[26] L. E. Erickson, Phys. Rev. B **19**, 4412 (1979).
[27] M. A. Teplov, Soviet Physics JETP **26**, 872 (1968).
[28] B. Bleaney, Physica (Utrecht) **69**, 317 (1973).
[29] A. Wokaun, S. C. Rand, R. G. Devoe, and R. G. Brewer, Phys. Rev. B **23**, 5733 (1981).
[30] T. Blasberg and D. Suter, J. Lumin. **65**, 199 (1995).
[31] R. Klieber, Ph.D. thesis, Universität Dortmund (2006).
[32] K. Holliday, M. Croci, E. Vauthey, and U. P. Wild, Phys. Rev. B **47**, 14741 (1993).
[33] S. Geller and E. Wood, Acta Crystallogr. **9**, 563 (1956).
[34] R. Diehl and G. Brandt, Mat. Res. Bull. **10**, 85 (1975).
[35] M. Mitsunaga, E. S. Kintzer, and R. G. Brewer, Phys. Rev. Lett. **52**, 1484 (1984).
[36] R. W. Equall, R. L. Cone, and R. M. Macfarlane, Phys. Rev. B **52**, 3963 (1995).
[37] H. Goldstein, C. P. Poole, and J. L. Safko, *Classical Mechanics* (Addison Wesley, San Francisco, 2002), p. 638.
[38] We use the common "zyz" notation for the Euler angles.
[39] M. Lovrić, P. Glasenapp, D. Suter, B. Tumino, A. Ferrier, P. Goldner, M. Sabooni, L. Rippe, and S. Kröll, Phys. Rev. B **84**, 104417 (2011).
[40] J. Mlynek, N. C. Wong, R. G. DeVoe, E. S. Kintzer, and R. G. Brewer, Phys. Rev. Lett. **50**, 993 (1983).
[41] N. C. Wong, E. S. Kintzer, J. Mlynek, R. G. Devoe, and R. G. Brewer, Phys. Rev. B **28**, 4993 (1983).
[42] R. M. Macfarlane, R. M. Shelby, and R. L. Shoemaker, Phys. Rev. Lett. **43**, 1726 (1979).
[43] J. J. Longdell, A. L. Alexander, and M. J. Sellars, Phys. Rev. B **74**, 195101 (2006).
[44] S. Kirkpatrick, C. D. Gelatt, and M. P. Vecchi, Science **220**, 671 (1983).
[45] M. Mitsunaga, E. S. Kintzer, and R. G. Brewer, Phys. Rev. B **31**, 6947 (1985).
[46] R. Klieber, A. Michalowski, R. Neuhaus, and D. Suter, Phys. Rev. B **67**, 184103 (2003).
[47] T. Blasberg and D. Suter, Opt. Commun. **120**, 55 (1995).
[48] R. Klieber and D. Suter, Phys. Rev. B **71**, 224418 (2005).
[49] L. Rippe, M. Nilsson, S. Kröll, R. Klieber, and D. Suter, Phys. Rev. A **71**, 062328 (2005).